Applied Thermal Engineering 208 (2022) 118147

Contents lists available at ScienceDirect

Applied Thermal Engineering

journal homepage: www.elsevier.com/locate/ate

Research paper

Hybrid model-based online estimation of air temperature in mobile small-scale cooling chambers

Markus Fallmann *, Agnes Poks, Martin Kozek

TU Wien, Institute of Mechanics and Mechatronics, Getreidemarkt 9, 1060 Vienna, Austria

ARTICLE INFO

Keywords:
Model-based estimation
Kalman filter
Hybrid system
Physical modeling
Gray-box modeling
Refrigeration

ABSTRACT

Mobile, small-scale refrigeration applications for last-mile deliveries have gained increased importance in recent years. As they face disturbances and frequent door openings more extensively than long-distance transport, reliable temperature information is crucial for control concepts to comply with temperature regulations and increase efficiency. For desired ruggedness, sensors are typically integrated within the cooling unit, yielding substantial deviations between actual air temperature in the cooling chamber and measured one — particularly in periods of altered airflow conditions resulting from fan switching and the actual door opening status. This article introduces and compares two hybrid, online estimation procedures to overcome this issue: firstly, a Kalman-filter approach based on a simple lumped physical heat transfer model, and secondly, a gray-box-model approach resulting from a realizable inversion of the physical model. Experimental investigations of typical operating profiles provide 14 h of real-world data to parameterize (11.75 h data length), validate (2.25 h data length), and compare both estimators. The proposed concepts are based on a sensor setup available in state-of-the-art system architectures and provide satisfactory temperature estimates with more than 83 % overall fit. As the algorithms provide comprehensive process insight independent of the actual operating condition, sophisticated control schemes can be built upon the concept.

1. Introduction

Refrigerated road transport plays a crucial role in the global cold chain. In total, the global refrigerated transport market amounted to roughly 15 billion USD in 2019 and is estimated to increase up to 23 billion USD in 2027 [1]. A share of more than 40 % of it refers to the road segment, indicating its paramount significance not just for supply in particular but also for its impact in terms of wasted goods. Thereby, a food loss of about 1.3 billion tons arise yearly, while a considerable amount of it can be traced back to insufficient temperature conditions during transport [2].

To inhibit or at least decrease waste of goods, it is essential to keep cargo temperature within a specific temperature range, regardless of any disturbances and in the face of significant influence by door openings during loading and unloading [3,4]. Especially small-scale refrigerated trucks are more exposed to disturbances and encounter door openings more frequently than large applications during long-distance supply. Due to increasing demand for home delivery in the future, last-mile transportation and, therefore, small-scale refrigerated trucks will rise in importance.

Hence, accurate control is necessary to attain sufficient temperature conditions [5–7]. Although the primary objective relates to the temperature of the goods, high expenses for appropriate measurement equipment, required ruggedness, and desired flexibility in fast-paced, small-scale transportation render actual cargo temperatures inaccessible in practical applications. Rather than that, temperature sensors are usually safely mounted in the cooling unit itself. Therefore, the temperature of the air within the cooling chamber substitutes for the initially intended control variable. Many state-of-the-art systems achieve a continuous and sufficiently distinctive air mixing in the chamber by a constantly running fan, allowing temperature sensors in the cooling unit to measure representative values. However, these measurements show severe deviations from the real temperature inside the cooling chamber if no such airflow is apparent [8,9]. Sophisticated control strategies that also consider energy consumption tend to turn off the fan and force the system to run in such operating modes more regularly than standard control approaches. This is particularly relevant if flexible secondary-loop refrigeration units [10] are used. Unawareness of the actual temperature during those periods would entail unreasonable control actions often captured by heuristic and, therefore, suboptimal remedies [11,12].

* Corresponding author.
E-mail address: markus.fallmann@tuwien.ac.at (M. Fallmann).

https://doi.org/10.1016/j.applthermaleng.2022.118147
Received 18 October 2021; Received in revised form 18 January 2022; Accepted 27 January 2022
Available online 22 February 2022

Nomenclature

Latin letters

a	Eigenvalue
$\boldsymbol{A}$	System matrix
$\boldsymbol{b}$	Input vector
$\boldsymbol{c}$	Output vector
C	Heat capacity
$\boldsymbol{d}$	Vector of continuous hybrid-estimator inputs
f	State equation
$\boldsymbol{G}$	Input matrix for process noise
i	Counter variable
$\boldsymbol{I}_2$	2×2 identity matrix
j	Counter variable
$\boldsymbol{J}$	Objective function
$\mathcal{J}$	Set of time steps constituting transition into mode 1
k	Time step, normalized time = t/T_s
kA	Heat transition coefficient
K	Compact parameter of the physical model
$\boldsymbol{K}_\mathrm{kf}$	Kalman-gain matrix
l	Counter variable
$\mathcal{L}$	Set of time steps constituting transition into mode 3
m	Operating mode
n	Number of time steps constituting mode transition
n_k	Number of samples in data set
n_S	Number of training data sets
n_V	Number of samples within both validation data sets
$\boldsymbol{P}$	Covariance matrix of estimation error
Q	Variance of process noise
$\boldsymbol{Q}$	Covariance matrix of process noise
$\dot{Q}$	Heat flow
r	Residual
R	Variance of measurement noise
S	Training data set
t	Continuous time
t_i	Continuous time at sampling instant i
T	Time constant
T_s	Sampling time
u	Input
$\boldsymbol{u}$	Vector of Inputs
v	Measurement noise
w	Process noise
$\boldsymbol{w}$	Vector of process noise
x	State
$\boldsymbol{x}$	State vector
y	Output

Greek letters

$\boldsymbol{\delta}$	Vector of binary hybrid-estimator inputs
Δ	Difference
$\boldsymbol{\epsilon}$	Vector of estimation error
$\boldsymbol{\zeta}$	Parameter vector of gray-box model
ϑ	Temperature
$\boldsymbol{\theta}$	Parameter vector of physical model
$\varkappa$	Parameter of gray-box model
$\boldsymbol{\Phi}$	Set of performance parameters

Subscripts and superscripts

cc	Cooling chamber
d	Discrete time
door	Door opening
fan	Air chiller fan
gb	Gray-box model
gly	Glycol
hygb	Hybrid gray-box-model approach
hykf	Hybrid Kalman-filter approach
i23	Initialization in/transition into mode 2 or 3
in	Inflowing position
init	Initial
kf	Kalman filter
meas	Measured
out	Outflowing position
t1	Transition into mode 1
t3	Transition into mode 3

Accents

$\tilde{z}$	Prediction of z
$\hat{z}$	Correction/estimate of z
z^*	Optimized value of z
$\bar{z}$	Mean of z

Acronyms

EKF	Extended Kalman filter
hygb	Hybrid gray-box-model
hykf	Hybrid Kalman-filter
RMSE	Root-mean-square error

Mathematical notation

$\mathbb{N}$	Natural numbers
$\mathbb{N}_0$	Natural numbers including 0
$\mathbb{R}$	Real numbers
$\mathbb{R}_{\geq 0}$	Positive real numbers including 0
$\mathcal{N}$	Gaussian distribution
$\mathrm{diag}\left[z_1, \ldots, z_n\right]$	Matrix with elements $z_1, \ldots, z_n$ on its diagonal
$\mathrm{Var}\left[\boldsymbol{z}\right]$	Covariance matrix of $\boldsymbol{z}$
$\dot{z}$	Time derivative of z (continuous time system)
$\boldsymbol{z}^\mathrm{T}$	Transpose of $\boldsymbol{z}$
$\boldsymbol{Z}^{-1}$	Inverse of matrix $\boldsymbol{Z}$

This work presents and compares two model-based, online estimation approaches to overcome this inaccessibility and to provide adequate knowledge about the actual temperature, enabling energy-optimal control in all operating modes. The need to differentiate between conditions based on binary inputs, i.e., the fan and the door opening, renders the overall estimators hybrid [13] and requires handling operating modes individually. Besides a Kalman-filter approach [14] based on a physically motivated model, a gray-box-

model approach [15] is additionally presented. Both rely on the same simple sensor setup located inside the cooling unit and available in the better part of state-of-the-art practical applications. Real-world experimental data drive parametrization and validation of the overall concepts. The proposed estimation processes indicate satisfactory temperature estimates and are easy to implement in already existing microcontrollers. The lucid and computationally simple mathematical background facilitates wide utilization even in low-cost applications.

Originating from process control, model-based estimation approaches [16–20] have gained increased interest in the last decades and have been utilized in numerous applications in a large number of fields. However, its combination with a hybrid system model has only been studied in recent years, predominantly by the pharmaceutical [21,22] and chemical [23,24] sectors. Although model-based estimation approaches are prevalent in process control, just little was done for temperature estimation or thermodynamic systems in general.

An autoregressive exogenous model served in [25,26] to gain temperature estimates of ceramic parts and an inaccessible measuring point in a coffee machine, respectively. Compared with that, the modeling approach proposed hereinafter is physically motivated and allows a more comprehensive insight into the system dynamics. Besides the established gray-box model being operated in the same feedforward fashion as in the mentioned literature sources, the applied Kalman filter differs by its natural feedback-based algorithm. While Beghi and Cecchinato [27] also used a standard Kalman filter, their application aims for a different estimated value, namely, the plant thermal load. In addition to that, they used this value to feed an adaptive and energy-efficient control approach. Despite the simplicity and easy-to-implement character of the standard Kalman filter, the extended and unscented version is utilized for model-based estimation more extensively in the literature. Enhanced ability to handle nonlinear systems by such approaches inevitably comes with increased complexity and higher effort for design and maintenance. However, Fux *et al.* [28] introduced an extended Kalman filter (EKF) that estimates model parameters and, therefore, allows to predict heat demands in buildings. Similar to that is the estimation of the thermal load and infiltration resistance in buildings by an EKF, shown in [29,30], respectively. While those publications focused on estimating demands, not temperatures, the presented work relies on a linear system description and thus applies the classic Kalman methodology. By contrast, O'Neill and Narayanan [31] proposed an EKF-based estimator for the actual temperature in supermarket refrigeration systems based on a comprehensive analytical model. Unscented Kalman filters based on gray-box models were utilized in [32,33] to provide estimates of building model parameters to predict energy consumption subsequently. Compared with what was done in literature, the hybrid architecture of the methods described in this work combined with the physically motivated model and the aim to estimate actual temperate values stand out.

While this paper focuses on the air temperature inside cooling chambers to serve high flexibility demanded in small-scale refrigerated trucks, some authors presented estimation methods to capture cargo temperature directly. Raval *et al.* [34] proposed a white-box model to estimate the temperature of oranges in closed rectangular food packages during transient cooling. A similar setup with a single product type and a closed shipping container is handled in [35] by an artificial neural network, the Kriging method, and the capacitive heat transfer method. Also, Emenike *et al.* [36] introduced a neural network approach to gain worst-case in-cargo temperature estimates using radio-frequency-identification-based sensing techniques. Without additional measurement equipment and based on a white-box model and continuous estimation of a characteristic time constant, Pedersen *et al.* [37] established an algorithm to estimate food temperature in supermarket display cases. As all these methods either rely on a single product type, a large variety of parameters necessary to know beforehand, expensive and sensitive additional measurement setups, or some combinations of these restrictions, they are not applicable for the intended purpose of last-mile transportation. Handling many different goods simultaneously and an amount of cargo varying with time due to loading and unloading sequences renders estimation of food temperature thereby impracticable.

Therefore, the importance of reliable estimates for air temperature inside the cooling chamber during all operating modes is apparent. Since state-of-the-art system architectures get along with simple measurements close to the cooling unit, flexibility introduced by more comprehensive control opportunities of secondary-loop refrigeration units remains unused. The presented strategies offer a more vivid process insight inevitably necessary to gain advantages regarding temperature control and simultaneously increase efficiency. It is with this so-gained knowledge about the actual temperature that sophisticated control concepts [13] can unfold their full potential. Compared with standard temperature sensors mounted close to the cooling unit, proposed estimation approaches provide more accurate temperature information close to the cargo in any operating condition. Thereby, such enhanced data pave the way for control strategies to cover the ultimate control target, the temperature of the goods, in a more appropriate fashion. Better process insight allows diminishing safety margins in the temperature control task compared with standard strategies, resulting in higher flexibility and reduced energy input. Besides that, purely heuristic control actions become needless as validated temperature data are available throughout all operation modes. Since optimized inputs may substitute them, efficiency is further improved. By providing an estimate to the control law in every time step by proposed algorithms, decision making relies on an improved data set and, therefore, yields more efficient and more reliable control actions.

The remainder of the paper is organized as follows: First, Section 2 outlines the system architecture and the measurement problem in detail. Introducing the physically motivated model in Section 3 is followed by the overall hybrid estimator design in Section 4. The Kalman-filter approach and the gray-box-model approach are described extensively in Sections 5 and 6, respectively. Next, Section 7 summarizes the experimental investigation, numerical results of the parametrization of the hybrid estimator approaches, and chosen performance parameters. Comprehensive validation with real measurement data and discussion complete these considerations. Finally, a brief outlook and limitations of the approaches are given in Section 8.

2. Detailed problem description

The considered system is a refrigerated truck with a small-scale cooling chamber, see Fig. 1. The part of the cooling unit situated within the chamber (detail A) contains an air–fluid heat exchanger and an air fan used to improve heat transfer by inducing forced convection. Evolved airflow conditions depend on whether the door is open or closed and whether the fan is on or off. Please note that the given setup precludes continuous fan speed change, rendering the related input solely binary. For ease of readability, Table 1 assigns physically meaningful operating modes to combinations of the binary system inputs, i.e., fan switch s_{fan} and door opening s_{door}, where $s_i \in \{0, 1\}$, $i \in \{\text{fan}, \text{door}\}$ holds.

Table 1
Classification of operating modes based on flow conditions depending on the fan switch s_{fan} and the door opening event s_{door}. While 0 indicates that the fan is off or the door is closed, a value of 1 represents an active fan or an open door.

	$s_{\text{fan}} = 0$	$s_{\text{fan}} = 1$
$s_{\text{door}} = 0$	Mode 3	Mode 1
$s_{\text{door}} = 1$	Mode 2	

An active fan forces the airflow to evolve independently of a door opening (mode 1). By contrast, a switched-off fan combined with an open door yields an airflow pointing in the opposite direction (mode 2). Please note that this is restricted to a positive temperature gradient from inside to outside the cooling chamber [8,9]. Finally, local

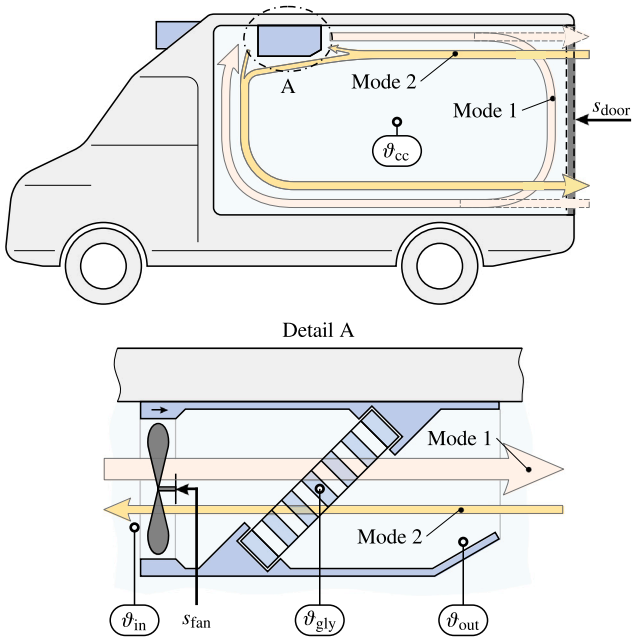

Fig. 1. Schematic illustration of a refrigerated truck with a small-scale cooling chamber, displaying vital temperature measurement points ϑ, binary system inputs s, and airflow conditions for different operating modes, indicated by thick arrows (see Table 1 for mode classification). In mode 1, the dashed arrow indicates flow condition in case of an open door. The airflow in operating mode 3 is internally driven by local temperature differences and therefore neglected within this graph. The small arrow above the fan in detail A indicates its flow direction if switched on.
Temperatures: air inside cooling chamber ϑ_{cc}, air at inflowing position ϑ_{in}, glycol inside air chiller ϑ_{gly}, air at outflowing position ϑ_{out}.
Binary inputs: door opening s_{door}, fan switch s_{fan}.

temperature differences remain the main driving force if the door is closed and the fan is off (mode 3). Therefore, resulting airflow is sensitive to the initial temperature distribution and a general illustration unenforceable.

The cooling unit mounted in the investigated refrigerated truck possesses an extended structure compared with classic approaches, see Fig. 2. Besides a standard cooling loop using propane as its coolant, it comprises an additional so-called storage loop running with a water–glycol mixture. This extension offers vast opportunities in general [10], but also for sophisticated control schemes aiming towards temperature-related objectives as well as higher efficiency.

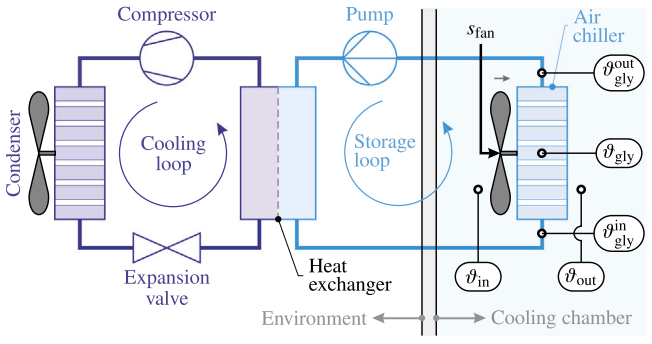

Fig. 2. Basic structure of the cooling unit utilized in the investigated refrigeration application. It consists of (left) a classic cooling loop using propane as its coolant and (right) a storage loop filled with a water–glycol mixture. The schematic displays vital temperature measurement points ϑ and the fan switch s_{fan}. The small arrow above the fan indicates its flow direction if switched on.
Temperatures: air at inflowing position ϑ_{in}, air at outflowing position ϑ_{out}, glycol flowing into air chiller ϑ^{in}_{gly}, glycol inside air chiller ϑ_{gly}, glycol flowing outside air chiller ϑ^{out}_{gly}.

Although the main objective is to keep the cargo temperature in a specific range, appropriate measurement data are rarely available in real applications. A heuristic way to compensate for this lack of information is to consider cargo temperatures indirectly by controlling the temperature of the air inside the cooling chamber ($\vartheta_{cc} \in \mathbb{R}$), Fig. 1. Mounting a temperature sensor in such an exposed position is practically unreasonable. As real circumstances demand a cost-effective and more robust way to track temperatures, only very few safely attached sensors are available, which are inside or very close to the cooling unit frame. In the given setup, temperature measurements are available for air at the inflowing position ($\vartheta_{in} \in \mathbb{R}$), air at the outflowing position ($\vartheta_{out} \in \mathbb{R}$), glycol flowing into the air chiller ($\vartheta^{in}_{gly} \in \mathbb{R}$), and glycol flowing out of the air chiller ($\vartheta^{out}_{gly} \in \mathbb{R}$). Based on glycol measurements, the temperature of the glycol inside the air chiller ($\vartheta_{gly} \in \mathbb{R}$) can be approximated using the arithmetic mean according to

$$\vartheta_{gly} = \frac{1}{2}\left(\vartheta^{in}_{gly} + \vartheta^{out}_{gly}\right). \tag{1}$$

Additionally, binary sensors provide values for the door opening s_{door} and the fan switch s_{fan}.

A variety of state-of-the-art control approaches gets solely along with measuring ϑ_{in}, e.g., [5–7]. As long as the air fan is running, i.e., operating mode 1 is active, air flows in such a way to let ϑ_{in} be a reasonable approximate for ϑ_{cc}, see schematic airflow in Fig. 1. By contrast, if the fan is off, significantly different flow conditions evolve (operating modes 2 and 3), resulting in a substantial deviation of ϑ_{in} from ϑ_{cc}. Control approaches that use ϑ_{in} regardless of the current operating mode lack knowledge about actual circumstances during operating modes 2 and 3. Therefore, corresponding control actions are either unreasonable or adapted heuristically [11,12]. Since standard refrigeration applications only turn off the air fan in rare events, e.g., during door openings to reduce overall energy consumption, suboptimal control actions within these periods are often accepted.

However, as small refrigerated trucks tend to face door openings and therefore a switched-off fan more often than large ones, careful consideration of these periods becomes more critical. In addition to that, the exceptional architecture of the cooling unit with its storage loop reveals additional opportunities to switch off the fan. Although running the fan from time to time is required to prevent severe inhomogeneities in the temperature distribution, a sophisticated control scheme will drive the system into operating modes 2 and 3 more frequently. Therefore, knowledge about ϑ_{cc} in all operating modes is a necessary prerequisite. Only then, control algorithms can use the flexibility of the cooling unit to its full extent and improve efficiency, reduce wear, and keep track of temperature restrictions during the entire operation.

3. Physical temperature model

As mentioned above, the air temperature inside the cooling chamber ϑ_{cc} is inaccessible to direct measurement in real operation. Therefore, appropriate estimates $\hat{\vartheta}_{cc}(t; m) \in \mathbb{R}$, written in continuous time $t \in \mathbb{R}_{\geq 0}$, for all three operating modes $m \in \{1, 2, 3\}$ are needed. Please note that explicitly stated mode dependencies of quantities allow handling relationships for all modes by a single notation in an easy-to-read manner. Although m is time-variant, i.e., $m = m(t)$, this dependency is only considered implicitly for the sake of brevity. However, explicit indication is done in some places to solve ambiguities. Hereinafter, nomenclature considers that model parameters, states, and outputs (partially) exhibit mode dependencies, while model inputs, true values, and measured values are inherently independent of any change in m.

While flow conditions in operating mode 1 allow a simple approach according to

$$\hat{\vartheta}_{cc}(t; 1) = \vartheta_{in}(t), \tag{2}$$

airflows in operating modes 2 and 3 call for more detailed considerations, see Fig. 1. For this purpose, a physically reasonable model for the relationship between ϑ_{cc}, ϑ_{gly}, and ϑ_{out} in operating modes 2 and 3 is introduced in the following.

3.1. Model description

The water–glycol mixture in the air chiller (mean temperature ϑ_{gly}) and the air inside the cooling chamber (temperature ϑ_{cc}) possess significantly higher heat capacities than the air volume close to the sensor measuring ϑ_{out}, see Fig. 1. Based on that, a simple lumped model of the given circumstances assumes ϑ_{out} to result from ϑ_{gly} and ϑ_{cc}, neglecting a reverse influence, see Fig. 3.

As the considered measuring point for ϑ_{cc} is located inside the cooling chamber, a noticeable difference between the temperature rise at this very point and the doorway in case of an open door will occur. A more comprehensive evaluation of the arising temperature distribution would be possible by Computational Fluid Dynamics analysis [8,9]. However, on the one hand, it would be computationally too expensive and, on the other hand, hard to incorporate into a control strategy calling for a single temperature value. However, the methodology presented in this work can be implemented for any specific measuring point inside the cooling chamber and, therefore, offers the opportunity to provide a more distributed insight by appropriately implementing several estimators for different locations. This can be especially helpful if sensitive cargo is placed close to the door and must be kept within a specific temperature range. Adding constraints in a sophisticated control scheme may incorporate this additional model-based information.

An energy balance describes this first-order model for modes $m \in \{2,3\}$ according to

$$C(m)\frac{d\,\vartheta_{out}(t;m)}{dt} = \dot{Q}_{gly}(t;m) + \dot{Q}_{cc}(t;m), \tag{3}$$

where $C \in \mathbb{R}$ is the heat capacity of the air with temperature ϑ_{out} and $\dot{Q}_{gly} \in \mathbb{R}$ and $\dot{Q}_{cc} \in \mathbb{R}$ are the heat flows through the corresponding walls. As heat flows result from temperature differences between each side of the walls, (3) can be rewritten as

$$\begin{aligned} C(m)\frac{d\,\vartheta_{out}(t;m)}{dt} &= (kA)_{gly}(m)\left[\vartheta_{gly}(t) - \vartheta_{out}(t)\right] + \cdots \\ &\quad (kA)_{cc}(m)\left[\vartheta_{cc}(t) - \vartheta_{out}(t)\right] \end{aligned} \tag{4}$$

with heat transition coefficients $(kA)_{gly} \in \mathbb{R}_{\geq 0}$ and $(kA)_{cc} \in \mathbb{R}_{\geq 0}$ of the walls separating the water–glycol mixture and the air inside the cooling chamber, respectively. The ideal heat transition, assumed within this modeling approach, comprises conduction and convection only. Due to the intended operation in the low-temperature regime, neglecting heat transfer through radiation is reasonable. Furthermore, although real circumstances may be better covered by a distributed rather than a lumped approach, its simplicity and eventually attained fit justify concentrating thermal masses in a single point and characterizing it by a single temperature value. Combining unknown model parameters yields the compact formulation

$$\begin{aligned} \frac{d\,\vartheta_{out}(t;m)}{dt} &= K_{gly}(m)\left[\vartheta_{gly}(t) - \vartheta_{out}(t)\right] + \cdots \\ &\quad K_{cc}(m)\left[\vartheta_{cc}(t) - \vartheta_{out}(t)\right], \end{aligned} \tag{5}$$

where $K_{gly}(m) \in \mathbb{R}_{\geq 0}$ and $K_{cc}(m) \in \mathbb{R}_{\geq 0}$ for $m \in \{2,3\}$ denote the four remaining unknown parameters.

Airflow induced by an open door in operating mode 2 renders the influence of ϑ_{gly} negligibly small (Fig. 1). Therefore, associated heat flow is omitted, yielding a reduced number of unknown parameters, see (6).

$$\dot{Q}_{gly}(t;2) \equiv 0 \;\Rightarrow\; (kA)_{gly}(2) = 0 \;\Rightarrow\; K_{gly}(2) = 0 \tag{6}$$

Parameter estimation methods, presented in Section 3.2, together with the recorded measurement data used for identification, shown in Fig. 9, yield appropriate model parameter estimates according to Table 3.

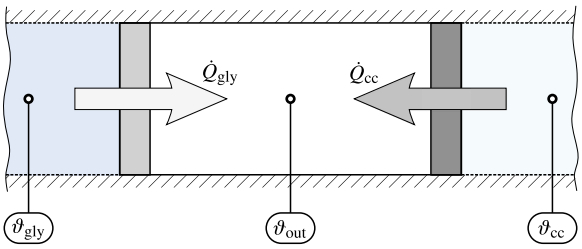

Fig. 3. Simple thermodynamic model of the evolution of the air temperature ϑ_{out} during operation in modes 2 and 3. Arrows represent heat flows $\dot{Q}$ through heat-conducting walls, while shaded boundaries indicate adiabatic ones.

3.2. Parameter estimation

Parametrization requires transforming (5) into an appropriate standard state–space formulation. With the state $x \in \mathbb{R}$ and the input vector $\boldsymbol{u} \in \mathbb{R}^2$, defined according to

$$x(t;m) := \vartheta_{out}(t;m), \;\; \boldsymbol{u}(t) := \begin{bmatrix} \vartheta_{gly}(t) \\ \vartheta_{cc}(t) \end{bmatrix}, \tag{7}$$

respectively, the state–space model for operating modes $m \in \{2,3\}$ is given by

$$\begin{aligned} \dot{x}(t;m) &= \left(-K_{gly}(m) - K_{cc}(m)\right)x(t) + \cdots \\ &\quad \begin{bmatrix} K_{gly}(m) & K_{cc}(m) \end{bmatrix}\boldsymbol{u}(t), \end{aligned} \tag{8a}$$

$$y(t;m) = x(t;m) = \vartheta_{out}(t;m), \tag{8b}$$

where a dot placed above a variable indicates a time derivative and $y \in \mathbb{R}$ denotes the model output.

Mode-wise aggregation of parameters into parameter vectors $\boldsymbol{\theta}(m) \in \mathbb{R}^2$ for $m \in \{2,3\}$ according to

$$\boldsymbol{\theta}(m) = \begin{bmatrix} K_{gly}(m) & K_{cc}(m) \end{bmatrix}^{\mathrm{T}} \tag{9}$$

results in the compact state–space formulation (10), where $f : \mathbb{R}^5 \to \mathbb{R}$ abbreviates the state equation.

$$\dot{x}(t;m) = f\left(x(t;m), \boldsymbol{u}(t); \boldsymbol{\theta}(m)\right) \tag{10a}$$

$$y(t;m) = x(t;m) \tag{10b}$$

Based on $n_S(m)$ experimentally gained training data sets $S_j(m)$, $j \in \{1,\ldots,n_S(m)\}$ including $n_k(S_j(m))$ samples each, the optimization problem

$$\boldsymbol{\theta}^*(m) = \underset{\boldsymbol{\theta}(m)}{\arg\min}\, J\left(\boldsymbol{\theta}(m)\right) \tag{11}$$

with the objective function $J \in \mathbb{R}$ according to

$$J\left(\boldsymbol{\theta}(m)\right) = \sum_{j=1}^{n_S(m)} \sum_{i=1}^{n_k(S_j(m))} \left[y(t_i;m) - y_{meas}(t_i)\right]^2 \tag{12}$$

yields the optimized parameter vectors $\boldsymbol{\theta}^*(m)$ for modes $m \in \{2,3\}$. Thereby, solving the state–space model (10) with inputs, which are given by the considered training data sets $S_j(m)$, and a parameter vector and subsequent sampling at sampling instances t_i result in the sampled simulated model output $y(m,t_i)$. Please note that the $\boldsymbol{\theta}$-dependency of $y(m,t_i)$ is stated implicitly by its mode-dependency. Minimizing the objective function (12) induces an estimated parameter vector that minimizes the squared difference between the simulated y and the experimentally measured output y_{meas} [38,39]. This work used MATLAB R2020a's System Identification Toolbox [40] to solve the optimization problem (11).

3.3. Basic problem of estimating ϑ_{cc}

Rearranging the dynamic model equation (5) according to (13) reveals that it lacks direct usage for estimating the temperature inside the cooling chamber: the required time derivative renders the problem noncausal.

$$\vartheta_{cc}(t;m) = \frac{1}{K_{cc}(m)} \frac{d\,\vartheta_{out}(t)}{dt} + \cdots \left(1 + \frac{K_{gly}(m)}{K_{cc}(m)}\right) \vartheta_{out}(t) - \frac{K_{gly}(m)}{K_{cc}(m)} \vartheta_{gly}(t) \tag{13}$$

Transition into a discrete-time formulation and approximating the derivative by finite backward differences, on the one hand, restore computability but, on the other hand, increase its sensitivity to measurement noise drastically. To overcome this issue, subsequently proposed methods smooth out noise effects implicitly.

4. Hybrid estimator design

Since different (dynamic) relationships between actually measured sensor values and the desired value for the air temperature inside the cooling chamber characterize each of the three operating modes, the overall estimator has to distinguish between different estimation methods. Fulfilling this requirement yields a hybrid estimator scheme, see Fig. 4, whereby here, the term *hybrid* denotes systems including continuous and binary variables [13].

While every estimation method relies on (parts of) the vector of continuous inputs $\boldsymbol{d} \in \mathbb{R}^3$, the vector of binary inputs $\boldsymbol{\delta} \in \{0,1\}^2$ determines which method is currently active. Input vectors are structured as follows:

$$\boldsymbol{d}(k) = \begin{bmatrix} \vartheta_{in}(k) \\ \vartheta_{out}(k) \\ \vartheta_{gly}(k) \end{bmatrix}, \quad \boldsymbol{\delta}(k) = \begin{bmatrix} s_{door}(k) \\ s_{fan}(k) \end{bmatrix}. \tag{14}$$

In order to serve a practical implementation in a microcontroller, the overall estimator design is carried out in discrete time, with $k \in \mathbb{N}_0$ denoting the current time step.

If the system is operating in mode 1, the discrete-time version of (2) is applied. Therefore, the method for mode 1 results as follows:

$$\hat{\vartheta}_{cc}(k;1) = \vartheta_{in}(k). \tag{15}$$

Apart from that, methods for handling modes 2 and 3 rely on the physical model (5). The following sections present two approaches to solve the impracticality of using (13) to estimate ϑ_{cc} in those operating modes. While the hybrid Kalman-filter (hykf) approach (Section 5) explicitly incorporates the physical model (5) and its parametrization, the hybrid gray-box-model (hygb) approach (Section 6) builds on a filtered version of (13) and separately estimated parameters.

Since transitions between operating modes require time to form the mode-characteristic air flows, both approaches comprise additional features to improve performance during such short periods. They are shown within the following sections but are neglected in Fig. 4 to maintain clarity.

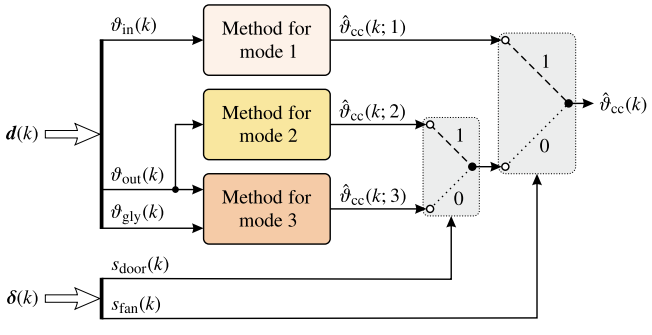

Fig. 4. Simplified representation of the discrete-time hybrid estimator scheme, valid for both estimation approaches. While the vector of binary inputs $\boldsymbol{\delta}$ selects the appropriate estimation method for the current operating mode, the method itself uses parts of the vector of continuous inputs $\boldsymbol{d}$ to provide the estimate $\hat{\vartheta}_{cc}$. For the sake of simplicity, features to improve the performance in the short period after a transition from one method to another are not depicted explicitly. Abbreviation k denotes the current time step.

5. Kalman-filter approach

Kalman filtering [14] is a state-of-the-art solution for state estimation, is applied in numerous practical applications, e.g., [27,41,42], and is well-covered in application-oriented literature [16,43]. Its simple structure further facilitates implementation and maintenance. Mode-dependent model parameters $\boldsymbol{\theta}(m)$ necessitate designing a separate filter for each mode $m \in \{2,3\}$.

5.1. Model description

To gain estimates $\hat{\vartheta}_{cc}$ based on model (5), the state vector for the Kalman-filter model $\boldsymbol{x}_{kf} \in \mathbb{R}^2$ represents an appropriately augmented version compared with (7):

$$\boldsymbol{x}_{kf}(t;m) = \begin{bmatrix} \vartheta_{out}(t;m) \\ \vartheta_{cc}(t;m) \end{bmatrix}. \tag{16}$$

Hence, the continuous-time state–space model results as

$$\dot{\boldsymbol{x}}_{kf}(t;m) = \boldsymbol{A}(m)\,\boldsymbol{x}_{kf}(t;m) + \boldsymbol{b}(m)\,u_{kf}(t) + \boldsymbol{G}\,\boldsymbol{w}(t;m) \tag{17a}$$

$$y_{kf}(t;m) = \boldsymbol{c}^{\mathrm{T}}\,\boldsymbol{x}_{kf}(t;m) + v(t) \tag{17b}$$

with the model input $u_{kf} \in \mathbb{R}$, the vector of process noise $\boldsymbol{w} \in \mathbb{R}^2$, the measurement noise $v \in \mathbb{R}$, the measurable model output $y_{kf} \in \mathbb{R}$, the system matrix $\boldsymbol{A} \in \mathbb{R}^{2\times2}$, the input vector $\boldsymbol{b} \in \mathbb{R}^2$, the input matrix for process noise $\boldsymbol{G} \in \mathbb{R}^{2\times2}$, and the output vector $\boldsymbol{c} \in \mathbb{R}^2$. While the model input is independent of the current mode m and chosen according to

$$u_{kf}(t) = \vartheta_{gly}(t), \tag{18}$$

evolution of the model output is mode-dependent, given as

$$y_{kf}(t;m) = \vartheta_{out}(t;m). \tag{19}$$

As in general, the considered system lacks detailed insight into the effects of process noises. Therefore, choosing

$$\boldsymbol{G} = \boldsymbol{I}_2 \tag{20}$$

with $\boldsymbol{I}_2$ denoting a 2×2 identity matrix is reasonable [43] and renders scalar components w_{out} and w_{cc} to solely act upon the dynamics of ϑ_{out} and ϑ_{cc}, respectively:

$$\boldsymbol{w}(t;m) = \begin{bmatrix} w_{out}(t;m) \\ w_{cc}(t;m) \end{bmatrix}. \tag{21}$$

Please note that noise processes are characterized in more detail in their discrete-time formulation, see (26) and (27). Reformulating model (5) by augmenting the state vector – see (16) – yields system matrix, input vector, and output vector to be given as

$$\boldsymbol{A}(m) = \begin{bmatrix} -K_{cc}(m) - K_{gly}(m) & K_{cc}(m) \\ 0 & 0 \end{bmatrix}, \tag{22}$$

$$\boldsymbol{b}(m) = \begin{bmatrix} K_{gly}(m) \\ 0 \end{bmatrix}, \quad \boldsymbol{c}^{\mathrm{T}} = \begin{bmatrix} 1 & 0 \end{bmatrix}. \tag{23}$$

To enable a digital implementation, discretization of the continuous-time state–space model (17) is necessary. Using a sampling time T_s and

zero-order hold on the input u_{kf} and the noise processes $\boldsymbol{w}$ and v yield the discrete-time formulation denoted by

$$\dot{\boldsymbol{x}}_{kf}(k;m) = \boldsymbol{A}_d(m)\,\boldsymbol{x}_{kf}(k;m) + \boldsymbol{b}_d(m)\,u_{kf}(k) + \boldsymbol{G}_d\,\boldsymbol{w}(k;m) \tag{24a}$$

$$y_{kf}(k;m) = \boldsymbol{c}_d^T \boldsymbol{x}_{kf}(k;m) + v(k), \tag{24b}$$

where subscript d indicates discrete-time quantities. Although

$$\boldsymbol{c}_d^T = \boldsymbol{c}^T \tag{25}$$

naturally holds, consistent indexing is utilized to solve otherwise possible ambiguities.

In practical applications, a common and sensible assumption is to model process noise and measurement noise being white, Gaussian distributed, and zero-mean. So, the mathematical formulation $\forall k \in \mathbb{N},\ m \in \{2,3\}$ is as follows:

$$\boldsymbol{w}(k;m) \sim \mathcal{N}(\boldsymbol{0}, \boldsymbol{Q}(k;m)), \tag{26a}$$

$$v(k) \sim \mathcal{N}(0, R(k)), \tag{26b}$$

where $\boldsymbol{Q} \in \mathbb{R}^{2\times2}$ and $R \in \mathbb{R}$ denote covariances of process noise and measurement noise, respectively. As measurement setup alone dictates measurement noise, v is independent of the current mode. By contrast, system dynamics and, hence, model uncertainties differ from mode to mode, calling for mode-dependent process noise.

Kalman filtering, in general, makes some further assumptions regarding noise processes [16]. Firstly, scalar process noises are uncorrelated, which means that

$$\boldsymbol{Q}(k;m) = \mathrm{diag}\left[Q_{out}(k;m), Q_{cc}(k;m)\right] \tag{27}$$

with $Q_{out} \in \mathbb{R}$ as the variance of w_{out} and $Q_{cc} \in \mathbb{R}$ as the variance of w_{cc} holds. Secondly, noise processes $\boldsymbol{w}$ and v are uncorrelated as well. This ensures the Kalman filter to be the optimal filter for such systems described above. Although these requirements seem restrictive, practical experience confirms real systems to fulfill them sufficiently. However, even if noise processes would deviate from the assumed Gaussian distribution, the Kalman filter would still be the optimal *linear* filter.

5.2. Filter formulation

Kalman-filter formulation is well-known from literature [14,16,43] and is, hereinafter, appropriately adapted for the given purpose. The filter comprises two stages: prediction and correction, whereby both are executed in every time step. A tilde ($\sim$) over a variable indicates predicted quantities, while corrected quantities exhibit a hat ($\wedge$) above. By defining estimation errors $\boldsymbol{\varepsilon} \in \mathbb{R}^2$ according to

$$\tilde{\boldsymbol{\varepsilon}}(k;m) := \boldsymbol{x}_{kf}(k) - \tilde{\boldsymbol{x}}_{kf}(k;m), \tag{28a}$$

$$\hat{\boldsymbol{\varepsilon}}(k;m) := \boldsymbol{x}_{kf}(k) - \hat{\boldsymbol{x}}_{kf}(k;m) \tag{28b}$$

with $\boldsymbol{x}_{kf}(k) \in \mathbb{R}^2$ as the true state vector, related covariance matrices $\boldsymbol{P} \in \mathbb{R}^{2\times2}$ are given by

$$\tilde{\boldsymbol{P}}(k;m) = \mathrm{Var}\left[\tilde{\boldsymbol{\varepsilon}}(k;m)\right], \tag{29a}$$

$$\hat{\boldsymbol{P}}(k;m) = \mathrm{Var}\left[\hat{\boldsymbol{\varepsilon}}(k;m)\right]. \tag{29b}$$

Utilizing these definitions enables stating estimator equations compactly. Predictions for the current time step rely on previously occurred inputs and calculated state estimates, see (30).

$$\tilde{\boldsymbol{x}}_{kf}(k;m) = \boldsymbol{A}_d(m)\,\hat{\boldsymbol{x}}_{kf}(k\text{-}1;m) + \boldsymbol{b}_d(m)\,u_{kf}(k\text{-}1) \tag{30a}$$

$$\tilde{y}_{kf}(k;m) = \boldsymbol{c}_d^T\,\tilde{\boldsymbol{x}}_{kf}(k;m) \tag{30b}$$

$$\tilde{\boldsymbol{P}}(k;m) = \boldsymbol{A}_d(m)\,\hat{\boldsymbol{P}}(k\text{-}1;m)\,\boldsymbol{A}_d^T(m) + \boldsymbol{G}_d\,\boldsymbol{Q}(k\text{-}1;m)\,\boldsymbol{G}_d^T \tag{30c}$$

Subsequently, corrected quantities originate from the difference $\Delta y_{kf}(k;m) \in \mathbb{R}$ between prediction $\tilde{y}_{kf}(k;m)$ and currently measured value $y_{kf}(k)$, given as

$$\Delta y_{kf}(k;m) = y_{kf}(k) - \tilde{y}_{kf}(k;m). \tag{31}$$

Then, the correction step can be written as follows:

$$\hat{\boldsymbol{x}}_{kf}(k;m) = \tilde{\boldsymbol{x}}_{kf}(k;m) + \boldsymbol{K}_{kf}(k;m)\,\Delta y_{kf}(k;m) \tag{32a}$$

$$\hat{y}_{kf}(k;m) = \boldsymbol{c}_d^T\,\hat{\boldsymbol{x}}_{kf}(k;m) \tag{32b}$$

$$\hat{\boldsymbol{P}}(k;m) = \left[\boldsymbol{I}_2 - \boldsymbol{K}_{kf}(k;m)\,\boldsymbol{c}_d^T\right]\,\tilde{\boldsymbol{P}}(k;m) \tag{32c}$$

with the Kalman gain $\boldsymbol{K}_{kf} \in \mathbb{R}^2$ calculated according to

$$\boldsymbol{K}_{kf}(k;m) = \tilde{\boldsymbol{P}}(k;m)\,\boldsymbol{c}_d\left[\boldsymbol{c}_d^T\,\tilde{\boldsymbol{P}}(k;m)\,\boldsymbol{c}_d + R(k)\right]^{-1}. \tag{33}$$

Finally, the desired estimate for the air temperature inside the cooling chamber during operation in modes $m \in \{2,3\}$ is given by

$$\hat{\vartheta}_{cc}(k;m) = \begin{bmatrix} 0 & 1 \end{bmatrix}\,\hat{\boldsymbol{x}}_{kf}(k;m). \tag{34}$$

5.3. Filter existence and stability

While full state observability of the pair $(\boldsymbol{A}_d(m), \boldsymbol{c}_d^T)$ is sufficient for the existence of a Kalman filter, full state controllability of the pair $(\boldsymbol{A}_d(m), \boldsymbol{G}_d)$ and $\boldsymbol{Q}(k;m)$ being positive definite ensure asymptotic stability [16]. It is simple to show that the given setup meets both conditions if $\boldsymbol{Q}(k;m)$ is chosen appropriately.

5.4. Filter initialization

Every mode switch into, or an overall fresh start in, mode 2 or 3 triggers the associated Kalman filter to start working. An appropriate initialization is indispensable and also vital to ensure high performance of the overall estimator approach, as it takes previous estimates as well as mode characteristics into account.

In order to facilitate readability throughout the following consideration, initializing time steps are highlighted by the subscript "i23". More mathematically, this can be written as

$$\begin{aligned} &k = k_{i23} \\ &\Leftrightarrow \\ &(m(k) \in \{2,3\}) \wedge \left[(m(k\text{-}1) \neq m(k)) \vee (k = 0)\right], \end{aligned} \tag{35}$$

where $k = 0$ denotes the very first time step after booting.

At such a time step k_{i23}, predicted values ($\tilde{\boldsymbol{x}}_{kf}$ and $\tilde{\boldsymbol{P}}$) are either inaccessible or at least unreasonable to calculate using (30a) and (30c). Therefore, they have to be defined appropriately. The time-invariant matrix $\tilde{\boldsymbol{P}}_{init}$ serves to initialize the covariance:

$$\tilde{\boldsymbol{P}}(k_{i23}; m(k_{i23})) = \tilde{\boldsymbol{P}}_{init}(m(k_{i23})). \tag{36}$$

By contrast, initializing the predicted state vector requires distinguishing whether the hybrid estimator starts freshly ($k_{i23} = 0$) or previously obtained estimates are already available:

$$\tilde{\boldsymbol{x}}_{kf}(k_{i23}; m(k_{i23})) = \begin{cases} \begin{bmatrix} \vartheta_{out}(0) \\ \vartheta_{in}(0) \end{bmatrix} & \text{if } k_{i23} = 0 \\ \begin{bmatrix} \vartheta_{out}(k_{i23}) \\ \hat{\vartheta}_{cc}(k_{i23}; m(k_{i23}\text{-}1)) \end{bmatrix} & \text{otherwise,} \end{cases} \tag{37}$$

where $\vartheta_{out}(0)$, $\vartheta_{in}(0)$, and $\vartheta_{out}(k_{i23})$ denote current measurement values. While the first state is, in fact, measurable and therefore simple to initialize, the prediction of the second state is either approximated by the estimate done in the previous time step or by the temperature of the air at the inflowing position. Coming from an uncertain level of knowledge at those initialization time steps, these are the best possible assumptions based on physical considerations of the system.

And finally, based on (37), $\tilde{y}_{kf}(k_{i23}; m(k_{i23}))$ results straightforward from (30b). Thus, all necessary quantities are known by now, allowing to continue estimation.

5.5. Mode transitions

Turning on the fan evokes operating mode 1, see Fig. 1. However, air flows require some time to evolve, yielding a transition period in which (15) is an unsatisfactory estimate. While this is apparent from experimental data for transitions into mode 1, transitions into other modes happen without such a significant characteristic.

To improve overall performance, (15) is adapted during a certain period (number of time steps $n_{\mathrm{t1}} \in \mathbb{N}$) after considered transitions. Associated transition time steps are highlighted by the subscript "t1" and defined as follows:

$$k = k_{\mathrm{t1}} \;\Leftrightarrow\; (m(k) = 1) \wedge (m(k\text{-}1) \neq m(k)) \,. \tag{38}$$

For all time steps $j \in \mathcal{J}$ given as

$$\mathcal{J} = \left\{ k \mid k_{\mathrm{t1}} \leq k \leq k_{\mathrm{t1}} + n_{\mathrm{t1}} - 1 \right\}, \tag{39}$$

a discrete-time first-order low pass, see (40), with time constant T_{t1} substitutes the originally defined estimator (15) for mode 1.

$$\hat{\vartheta}_{\mathrm{cc}}(j;1) = \hat{\vartheta}_{\mathrm{cc}}(j\text{-}1;1) + \frac{T_{\mathrm{s}}}{T_{\mathrm{t1}}} \left[\vartheta_{\mathrm{in}}(j\text{-}1) - \hat{\vartheta}_{\mathrm{cc}}(j\text{-}1;1) \right] \tag{40}$$

However, because previously estimated values are necessary for applying the low-pass strategy, (15) still covers booting in mode 1. Therefore, (38) neglects $k_{\mathrm{t1}} = 0$ as a possible solution.

5.6. Parameters

Parameters to influence the performance of the overall hykf approach can concisely be written as the set $\boldsymbol{\Phi}_{\mathrm{hykf}}$:

$$\boldsymbol{\Phi}_{\mathrm{hykf}} = \left\{ T_{\mathrm{s}},\; R,\; \boldsymbol{Q}(2),\; \boldsymbol{Q}(3),\; \tilde{\boldsymbol{P}}_{\mathrm{init}}(2),\; \tilde{\boldsymbol{P}}_{\mathrm{init}}(3),\; n_{\mathrm{t1}},\; T_{\mathrm{t1}} \right\}. \tag{41}$$

Note that real applications usually lack comprehensive insight into the process, inhibiting reasonable definitions of time-variant noise processes. Therefore, time-dependency is neglected. Section 7.4 presents the parameter values that are applied to the actually considered system.

5.7. Flow chart

The overall hykf approach consists of three strands, one for each mode, and additional procedures covering initialization and mode transitions. To summarize all considerations mentioned above, Fig. 5 outlines process steps and their interactions lucidly and provides references to relevant equations, facilitating implementation.

6. Gray-box-model approach

Gray-box models denote a class of mathematical descriptions that considers physical circumstances and appropriate adaptions resulting from iterative design and validation throughout the modeling procedure [15]. Such an approach, in general, allows developing well-fitting models by extending moderate insight into system dynamics by grasp gained from real measurement data. As these so-developed models provide more vivid analytical knowledge of process behavior than black-box models [38], they improve numerous technical and non-technical applications, e.g., [44,45].

Compared with the Kalman-filter approach comprising a prediction and a correction step, this approach provides a more direct way to estimate the air temperature inside the cooling chamber. It aims towards a simple discrete-time model directly usable for estimation.

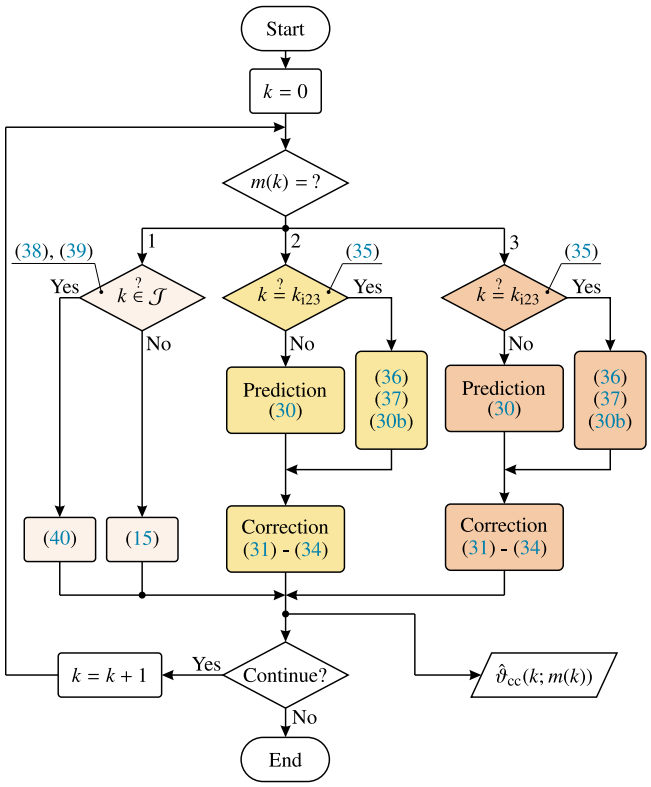

Fig. 5. Flow chart of the hybrid Kalman-filter approach, including references to all relevant equations.

6.1. Model description

Based on several adaptions of a discrete-time version of (13) and iterated identification and validation, the following physically motivated model for modes $m \in \{2, 3\}$ was obtained:

$$\begin{aligned} \vartheta_{\mathrm{cc}}(k;m) \quad =& \vartheta_{\mathrm{cc}}(k\text{-}1;m) + \cdots \\ & \frac{T_{\mathrm{s}}}{T_{\mathrm{gb}}(m)} \left[\varkappa_{\mathrm{out},1}(m)\, \vartheta_{\mathrm{out}}(k\text{-}1) + \cdots \right. \\ & \qquad \varkappa_{\mathrm{out},2}(m)\, \vartheta_{\mathrm{out}}(k\text{-}2) + \cdots \\ & \qquad \left. \varkappa_{\mathrm{gly}}(m)\, \vartheta_{\mathrm{gly}}(k\text{-}1) - \vartheta_{\mathrm{cc}}(k\text{-}1;m) \right], \end{aligned} \tag{42}$$

where $T_{\mathrm{gb}} \in \mathbb{R}$ is the time constant of the first-order low pass and $\varkappa_{\mathrm{out},1}, \varkappa_{\mathrm{out},2}, \varkappa_{\mathrm{gly}} \in \mathbb{R}$ denote gains of model inputs. For both modes, this yields eight unknown parameters in total. In mode 2, according to already previously mentioned circumstances (6), the influence of the glycol temperature vanishes. This results in

$$\varkappa_{\mathrm{gly}}(2) = 0 \tag{43}$$

to hold and finally seven parameters to be determined.

6.2. Parameter estimation

In order to perform standard parameter estimation techniques, it is sensible to transform model Eq. (42) into its discrete-time state–space formulation

$$x_{\mathrm{gb}}(k\text{+}1;m) = a_{\mathrm{gb}}(m)\, x_{\mathrm{gb}}(k;m) + \boldsymbol{b}_{\mathrm{gb}}^{\mathrm{T}}(m)\, \boldsymbol{u}_{\mathrm{gb}}(k) \tag{44a}$$

$$y_{\mathrm{gb}}(k;m) = x_{\mathrm{gb}}(k;m) = \vartheta_{\mathrm{cc}}(k;m) \tag{44b}$$

with the state $x_{\mathrm{gb}} \in \mathbb{R}$ and the vector of inputs $\boldsymbol{u}_{\mathrm{gb}} \in \mathbb{R}^3$ according to

$$x_{\mathrm{gb}}(k;m) := \vartheta_{\mathrm{cc}}(k;m), \quad \boldsymbol{u}_{\mathrm{gb}}(k) := \begin{bmatrix} \vartheta_{\mathrm{out}}(k) \\ \vartheta_{\mathrm{out}}(k\text{-}1) \\ \vartheta_{\mathrm{gly}}(k) \end{bmatrix}, \tag{45}$$

respectively, and the output $y_{gb} \in \mathbb{R}$. The eigenvalue $a_{gb} \in \mathbb{R}$ and the input vector $\boldsymbol{b}_{gb}^{T} \in \mathbb{R}^3$ are then given by (46a) and (46b), respectively.

$$a_{gb}(m) = \left[1 - \frac{T_s}{T_{gb}(m)}\right] \tag{46a}$$

$$\boldsymbol{b}_{gb}^{T}(m) = \frac{T_s}{T_{gb}(m)} \begin{bmatrix} \varkappa_{out,1}(m) & \varkappa_{out,2}(m) & \varkappa_{gly}(m) \end{bmatrix} \tag{46b}$$

Comprising model parameters in a mode-wise fashion by parameter vectors $\boldsymbol{\zeta}(m) \in \mathbb{R}^4$ for $m \in \{2,3\}$ according to

$$\boldsymbol{\zeta}(m) = \begin{bmatrix} T_{gb}(m) & \varkappa_{out,1}(m) & \varkappa_{out,2}(m) & \varkappa_{gly}(m) \end{bmatrix}^{T} \tag{47}$$

allows a compact state–space formulation as follows:

$$x_{gb}(k+1;m) = f_{gb}\left(x_{gb}(k;m), \boldsymbol{u}_{gb}(k), \boldsymbol{\zeta}(m)\right) \tag{48a}$$

$$y_{gb}(k;m) = x_{gb}(k;m), \tag{48b}$$

where $f_{gb} : \mathbb{R}^8 \to \mathbb{R}$ denotes the state equation.

Analogous to the parameter estimation of the physical model (Section 3.2) $n_S(m)$ experimentally gained training data sets $S_j(m)$, $j \in \{1, \dots, n_S(m)\}$ including $n_k(S_j(m))$ samples each constitute the experimental foundation for the – here appropriately adapted – optimization problem

$$\boldsymbol{\zeta}^*(m) = \arg\min_{\boldsymbol{\zeta}(m)} J_{gb}\left(\boldsymbol{\zeta}(m)\right) \tag{49}$$

with the objective function $J_{gb} \in \mathbb{R}$ given as

$$J_{gb}\left(\boldsymbol{\zeta}(m)\right) = \sum_{j=1}^{n_S(m)} \sum_{i=1}^{n_k(S_j(m))} \left[y_{gb}(i;m) - y_{meas}(i)\right]^2 \tag{50}$$

and subject to

$$T_{gb}(m) > T_s/2. \tag{51}$$

Note that the $\boldsymbol{\zeta}$-dependency of $y_{gb}(m,i)$ is stated implicitly by its mode-dependency. Parameter estimation [38,39] is done identically to Section 3.2 using MATLAB R2020a's System Identification Toolbox [40] and yields the optimal solutions $\boldsymbol{\zeta}^*(m)$ for modes $m \in \{2,3\}$.

In addition, restricting T_{gb} according to (51) ensures that the eigenvalue a_{gb} (46a) remains within the unit circle, providing asymptotic stability of the parametrized estimator.

6.3. Estimator formulation

The model Eq. (42) together with the eventually identified parameter vectors $\boldsymbol{\zeta}(m)$ yield the discrete-time estimator equation for the current time step k and for modes $m \in \{2,3\}$ as follows:

$$\begin{aligned} \hat{\vartheta}_{cc}(k;m) = {} & \hat{\vartheta}_{cc}(k\text{-}1;m) + \cdots \\ & \frac{T_s}{T_{gb}(m)} \left[\varkappa_{out,1}(m)\, \vartheta_{out}(k\text{-}1) + \cdots \right. \\ & \quad \varkappa_{out,2}(m)\, \vartheta_{out}(k\text{-}2) + \cdots \\ & \quad \left. \varkappa_{gly}(m)\, \vartheta_{gly}(k\text{-}1) - \hat{\vartheta}_{cc}(k\text{-}1;m)\right]. \end{aligned} \tag{52}$$

6.4. Estimator initialization

Suppose booting at $k = 0$ in operating mode 2 or 3, previous model inputs and the previous estimate are unavailable. Hence, the very first measured values replace previously unknown quantities according to (53).

$$\vartheta_{out}(\text{-}2) = \vartheta_{out}(0) \tag{53a}$$

$$\vartheta_{out}(\text{-}1) = \vartheta_{out}(0) \tag{53b}$$

$$\vartheta_{gly}(\text{-}1) = \vartheta_{gly}(0) \tag{53c}$$

$$\hat{\vartheta}_{cc}(\text{-}1;m) = \vartheta_{in}(0) \tag{53d}$$

While (53a) to (53c) are intuitive choices, (53d) represents the physically best possible approximation in the face of complete uncertainty of the past as it relies on the assumption that some sort of intermixing of the air has previously happened by the fan or otherwise.

6.5. Mode transitions

As the airflow evolution in mode 1 needs some time independently of the applied estimator approach, the same considerations for a transition into mode 1 as for the hykf approach hold here as well — see Section 5.5 for detailed explanation.

Besides that, the hygb approach requires another adaption because it lacks considering feedback during operation as the Kalman filter naturally does. Due to its feed-forward structure, rapidly-changing previous values would cause a severe performance decrease after transitioning into a mode with comparably slow dynamics (mode 3). Therefore, a zero-order model reasonably replaces estimator formulation (52) during a certain period (number of time steps $n_{t3} \in \mathbb{R}$) after such a transition. Formally written, with defining the time step in which a transition into mode 3 occurs $k_{t3} \in \mathbb{N}$ according to

$$k = k_{t3} \;\Leftrightarrow\; (m(k) = 3) \wedge (m(k\text{-}1) \neq m(k)). \tag{54}$$

the estimator (52) is replaced by the zero-order model

$$\hat{\vartheta}_{cc}(l;3) = \hat{\vartheta}_{cc}\left(l\text{-}1; m(l\text{-}1)\right) \tag{55}$$

for all time steps $l \in \mathcal{L}$ given as

$$\mathcal{L} = \left\{ k \mid k_{t3} \leq k \leq k_{t3} + n_{t3} - 1 \right\}. \tag{56}$$

Please note that booting in mode 3 calls for an appropriate initialization (Section 6.4) rather than this transition procedure. Therefore, (54) neglects $k_{t3} = 0$ as a possible solution.

6.6. Parameters

Apart from model-related parameters $\boldsymbol{\zeta}(m)$, the performance of the overall hygb approach depends on the set $\boldsymbol{\Phi}_{hygb}$, given by

$$\boldsymbol{\Phi}_{hygb} = \left\{T_s, n_{t1}, T_{t1}, n_{t3}\right\} \tag{57}$$

Please note the decreased number of influencing factors compared with the hykf approach (41), further emphasizing the simplicity of this approach.

Section 7.5 summarizes the model and performance parameters actually used for the considered system.

6.7. Flow chart

The overall hygb approach consists of three strands, one for each mode, and additional procedures covering initialization and mode transitions. To summarize the considerations mentioned above, Fig. 6 outlines process steps and their interactions lucidly and provides references to relevant equations, facilitating implementation.

7. Results and discussion

7.1. Experimental investigation

The experimental setup comprises a series-production truck adapted in small series for refrigeration purposes and additional equipment, allowing comprehensive investigations, see Fig. 7. The fan heater mounted on the floor of the cooling chamber enables emulation of reproducible heat flows but modifies the airflow conditions significantly. Because the actual airflow is vital for the relationship between measured temperature values at different locations, conducted experiments waive utilizing the fan heater to obtain data sets representative for real operation.

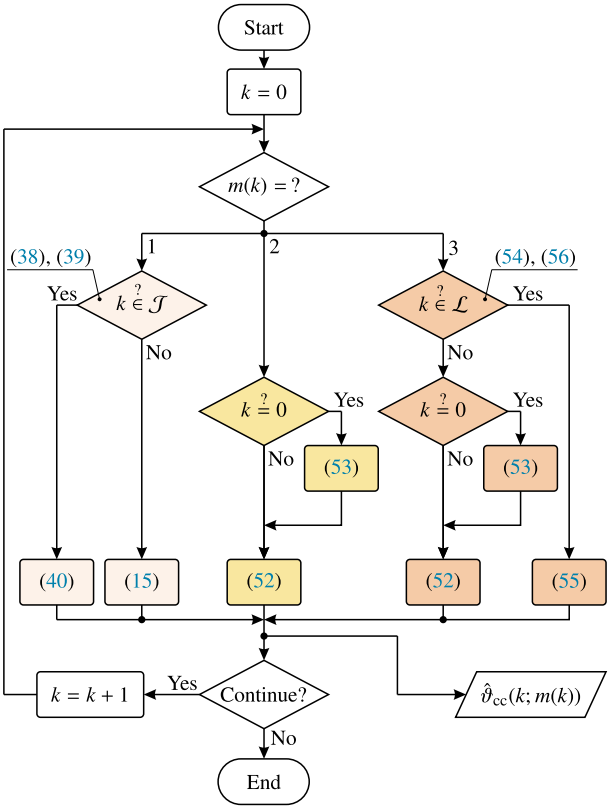

Fig. 6. Flow chart of the hybrid gray-box-model approach, including references to all relevant equations.

To gain deeper insight into realistic circumstances, empty cardboard boxes in a partially (Fig. 7 d) and completely filled setup (Fig. 7 e) simulate flow resistances. While their influence on temperature distribution remains negligibly small due to their insignificant thermal mass, their impact on the airflow is close to reality. Besides the parameters of the cardboard boxes, Table 2 provides a comprehensive overview of experimental conditions.

Table 2
Experimental conditions used for data acquisition.

Condition	Value
Sampling time	10 s
Sensors for	
$\vartheta_{in}, \vartheta_{out}, \vartheta_{gly}^{in}, \vartheta_{gly}^{out}$	Dallas DS18S20 [46]
ϑ_{cc}	3-wire Pt100 class B [47]
Accuracy for sensor	
Dallas DS18S20	±0.5 °C
3-wire Pt100 class B	±0.3 °C at 0 °C
Box	
Dimensions	65 cm x 35 cm x 37 cm
Volume	84 liters
Filling degree	
Empty (Fig. 7 c)	0 boxes
Partially filled (Fig. 7 d)	5 boxes
Completely filled (Fig. 7 e)	10 boxes
Door opening transition time	
To open	≈6 s
To close	≈1.5 s

Changing the number of boxes inside the cooling chamber, i.e., altering the filling degree, naturally comes with a door opening. Necessary human interaction to carefully arrange the boxes in a reproducible manner drastically limits data reliability and reproducibility during these periods. Therefore, those data sections are neglected in the following.

Fig. 7. Investigated refrigerated truck in (a) diagonal front view and (b) diagonal rear view. Its cooling chamber is shown in an empty, a partially filled, and a completely filled setup in (c)–(e), respectively. The fan heater, mounted on the floor of the cooling chamber and apparent from (c–e), is off throughout the whole experimental investigation within this work. Some areas of (a) and (b) are blurred for legal reasons.

Although door openings are handled manually, using a single operator allows comparable conditions throughout the experiments. To safely snap door wings, the transition time for opening is four times longer than for closing (Table 2).

The two-part door is asymmetrically divided and unblocks the entire cross section of the cooling chamber, see Fig. 8. Besides the dimensions of the overall chamber, the schematic shows the position of the sensor measuring ϑ_{cc}. Although its actual location is closer to the front wall than graphically depicted in Fig. 1, the presented methodologies apply to any arbitrarily chosen sensor position. However, preliminary test runs with several additional sensors within the cooling chamber confirmed operators' empirical knowledge of using the shown sensor position to obtain a representative measurement for the air temperature inside the cooling chamber.

To solely gain system insight without grasping any possible control dynamics, the setup was operated in a feedforward fashion during data collection, i.e., it was not controlled to fulfill any specific control target.

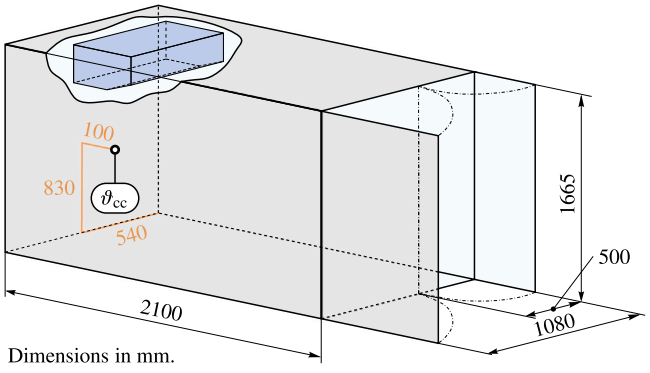

Fig. 8. Schematic and dimensions of the investigated small-scale cooling chamber and positioning of the sensor measuring the temperature ϑ_{cc} of the air inside the cooling chamber.

Thereby, the manipulated inputs were chosen to cover the input, state, and output range to map system behavior in a way representative of all kinds of operating conditions. The cooling load varied between 0 W and the maximum output of the cooling unit of 1200 W throughout the experiment.

Time-domain data for ϑ_{cc}, ϑ_{in}, ϑ_{out}, ϑ_{gly}^{in}, and ϑ_{gly}^{out} (see Figs. 1 and 2 for schematic sensor locations) are obtained by the setup described above.

7.2. Measured results

Two measurement data sets (Fig. 9) representative for the intended operating range of the investigated refrigerated system were obtained. Both are 7 h long and contain all relevant measured quantities, whereby, as an exception, ϑ_{gly} is calculated and results from arithmetic mean (1) based on measured inflow and outflow temperatures. For the sake of simplicity, binary inputs are neglected in the graphical display but are implicitly apparent from the operating modes presented by different background colors.

Besides door openings (mode 2), different operating strategies regarding the combination of running/shutting down the cooling unit during the fan is turned off are captured as well. While technical circumstances require running the pump when the compressor is on, turning on or off the fan is an independent input. Different system behavior in those operating conditions is apparent from a decreasing temperature ϑ_{gly} when the fan is off, and the compressor together with the pump is still running. Compared with that, ϑ_{gly} rises – at least slightly – if the compressor and pump are off during mode 2 or 3, see Fig. 9b.

The second measurement data set (Fig. 9b) also includes a comparison of three door-opening sequences carried out under equal system inputs but different filling degrees of the cooling chamber within the period from 0 to approximately 2.25 h. The differences between these three sequences are sufficiently small from a qualitative and quantitative perspective to justify the assumption to neglect the filling degree as an actual input of the estimator schemes. This experimental observation renders estimator reliability more robust because the filling degree is, in any case, difficult to access in practical applications. Although using standard containers together with a tracking system – realized either manually by the operator or automatically by, e.g., a camera system – would provide a more vivid insight, associated costs, personnel expenses, and reduced flexibility regarding transported goods prevent such systems from a broad application in the discussed small-scale refrigerated trucks.

While the better part of the measurement data serves for parametrization and, therefore, training, some sections are exclusively designated for validating the hybrid estimator concepts, see *Data Set I* and *Data Set II* shown in Fig. 9. With this allocation, parameter estimation for mode 2 relies on 5 and for mode 3 on 13 partial data sets. By contrast, overall validation data comprise 2 partial data sets with mode 2 and 6 with mode 3.

Furthermore, the partitioning is chosen in such a way as to keep validation data within the working range covered by training data, see Fig. 10. While deviations between ϑ_{cc} and ϑ_{in} in mode 2 and 3 (Figs. 10 c,d) point out the need for an appropriate dynamic estimator, relations in mode 1 (Fig. 10 b) confirm the simple approach (2) and eventually its discrete-time counterpart (15) to be a sensible estimation strategy within this operating condition. However, a few data points deviate from the 45° line. Because they are attributed to the short periods after a switch into mode 1, mode transition (40) guarantees reducing these unintended deviations and improves performance.

7.3. Physical model

Applying the proposed parameter estimation approach (Section 3.2) to experimentally-gained training data yields estimated parameter values for the physical model (5), see Table 3. Please note that estimated parameters are always stated by their estimated mean and estimated standard deviation within this work.

With the continuous-time eigenvalue $a(m)$ according to

$$a(m) = -\Big(K_{gly}(m) + K_{cc}(m)\Big), \tag{58}$$

one can immediately identify mode 2 to possess faster dynamics com-

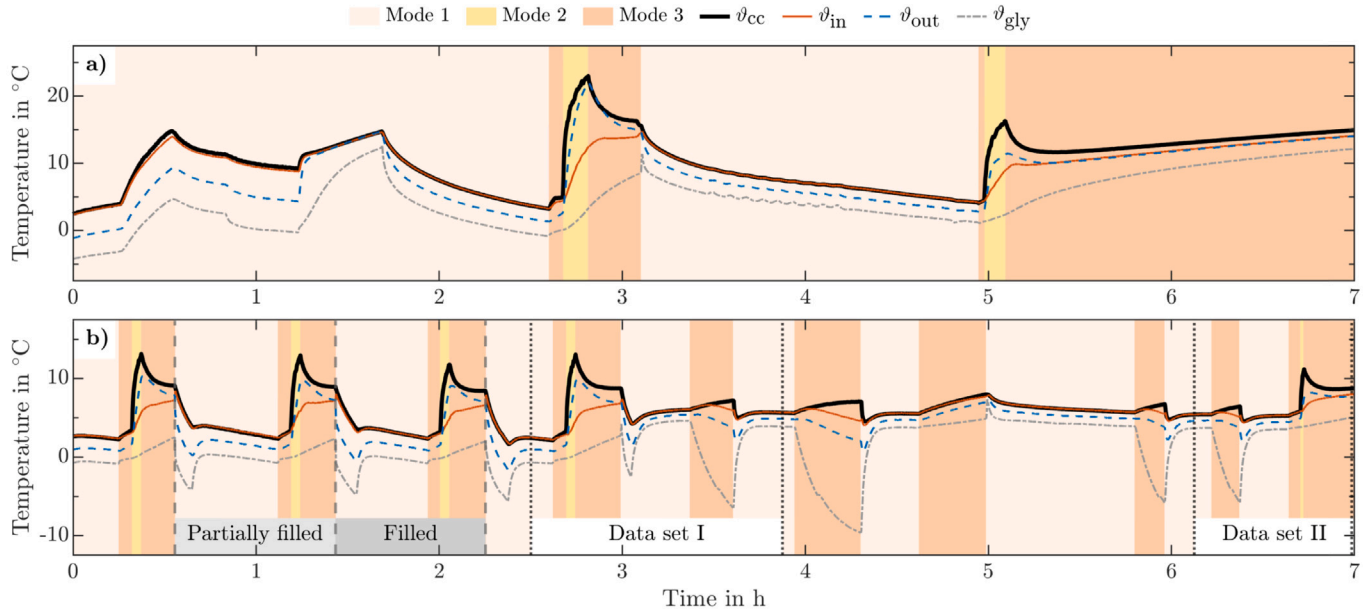

Fig. 9. Measurement data sets (a) and (b) acquired by utilizing the proposed experimental setup. Sections labeled as *Data set I* and *Data set II* are used for validation, while the remaining data are used for training. Appropriate labels indicate periods with a (partly) filled cooling chamber according to Fig. 7(d) and (e). Due to the exposed sensor setup in the experimental investigation, human interactions during loading and unloading of the cooling chamber drastically limit data reliability and reproducibility in those periods. Therefore, associated measurement data are excluded and graphically marked by dashed vertical lines.

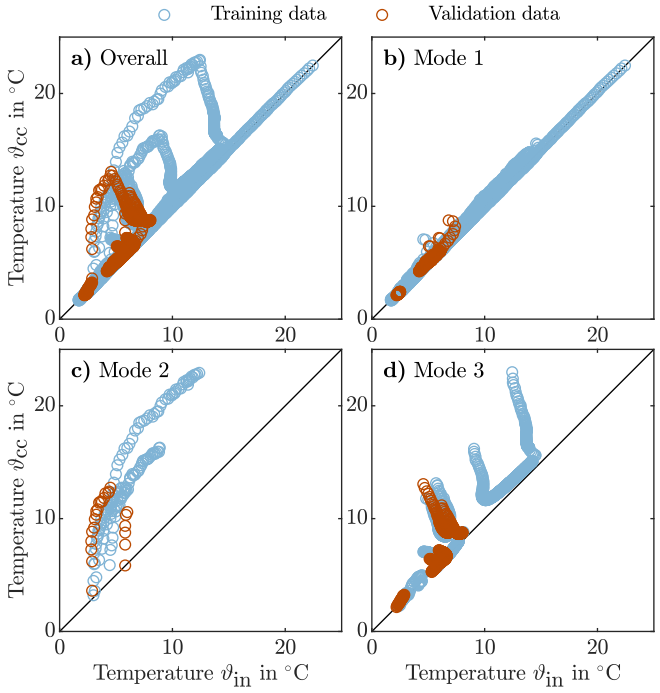

Fig. 10. Relation between air temperature inside the cooling chamber ϑ_{cc} and air temperature at the inflow position ϑ_{in}, depicted for (a) the overall measurement data and (b–d) each mode separately. Coloring indicates partitioning into training and validation data.

pared with mode 3. This is in accordance with the intuitive understanding that forced convection facilitates heat exchange.

Table 3
(Estimated) parameter values of the physical model.

Parameter	(Estimated) value	Unit
$K_{gly}(2)$	0[a]	s^{-1}
$K_{cc}(2)$	10.7 ± 0.1	$10^{-3}s^{-1}$
$K_{gly}(3)$	0.890 ± 0.037	$10^{-3}s^{-1}$
$K_{cc}(3)$	2.17 ± 0.16	$10^{-3}s^{-1}$

[a]Exact, not estimated — see (6).

7.4. Settings of the hybrid Kalman-filter approach

Besides the parameter vectors of the physical model $\boldsymbol{\theta}(m)$, $m \in \{2, 3\}$ with the elements according to Section 7.3, the hykf approach requires to additionally define the set of performance parameters $\boldsymbol{\Phi}_{hykf}$, see (41). While Table 4 summarizes its scalar quantities, associated matrices are given by (59).

The variance of measurement noise R results from sensor characteristics, and craving high performance on validation data dictates the parameters for transition into mode 1 (n_{t1}, T_{t1}).

$$\boldsymbol{Q}(2) = \begin{bmatrix} 0.01 & 0 \\ 0 & 2 \end{bmatrix} (°C)^2 s^{-2} \tag{59a}$$

$$\boldsymbol{Q}(3) = \begin{bmatrix} 0.15 & 0 \\ 0 & 10 \end{bmatrix} (°C)^2 s^{-2} \tag{59b}$$

$$\tilde{\boldsymbol{P}}_{init}(2) = \tilde{\boldsymbol{P}}_{init}(3) = \begin{bmatrix} 1 & 0 \\ 0 & 1 \end{bmatrix} (°C)^2 \tag{59c}$$

As the solely temperature-driven flow evolution in mode 3 is related to higher model uncertainties compared with the mainly externally driven flow in mode 2, the covariance matrix of process noise $\boldsymbol{Q}(3)$ possesses significantly higher diagonal elements than $\boldsymbol{Q}(2)$. Because there is no sensible reason for different certainty levels of the estimates immediately after a switch into mode 2 or 3, respectively, the initial covariance matrices of the estimation error related to prediction $\tilde{\boldsymbol{P}}_{init}(2)$ and $\tilde{\boldsymbol{P}}_{init}(3)$ are identical for both operating modes. Absolute values of the elements in (59) are chosen empirically to serve high overall performance.

Table 4
Values for the scalar performance parameters of the hybrid Kalman-filter approach.

Parameter	Value	Unit
T_s	10[a]	s
R	0.1	$(°C)^2$
n_{t1}	6	steps
T_{t1}	30	s

[a]According to experimental setup — see Table 2.

7.5. Settings of the hybrid gray-box-model approach

To fully specify the hygb approach, model-related parameter vectors $\boldsymbol{\zeta}(m)$ for $m \in \{2, 3\}$ - see (47) - and the vector of performance parameters $\boldsymbol{\Phi}_{hygb}$ - see (57) - have to be defined. Table 5 presents the estimated and chosen values.

Although the hygb approach exhibits more model-related parameters than the hykf approach, significantly fewer performance-related parameters render this overall method simpler. Furthermore, applying the simple restriction (51) during parameter estimation already ensures asymptotic stability, while it requires a more detailed examination to verify it for a Kalman filter — see Section 5.3.

Since the hygb and the hykf approach differ from each other only in mode 2 and 3, parameters for transition into mode 1 remain identical. Additionally, the hygb approach includes a supplemental method to handle transitions into mode 3, whereby the related parameter n_{t3} results empirically from analyzing overall performance for different values.

Table 5
Values for the model-related and performance parameters of the hybrid gray-box-model approach.

Parameter	(Estimated) value	Unit
$T_{gb}(2)$	33.4 ± 14.4	s
$\varkappa_{out,1}(2)$	13.5 ± 1.3	1
$\varkappa_{out,2}(2)$	-12.6 ± 1.3	1
$\varkappa_{gly}(2)$	0[a]	1
$T_{gb}(3)$	72.2 ± 11.2	s
$\varkappa_{out,1}(3)$	42.4 ± 2.5	1
$\varkappa_{out,2}(3)$	-41.0 ± 2.5	1
$\varkappa_{gly}(3)$	-0.469 ± 0.014	1
T_s	10[b]	s
n_{t1}	6	steps
T_{t1}	30	s
n_{t3}	3	steps

[a]Exact, not estimated — see (43).
[b]According to experimental setup — see Table 2.

7.6. Validation of hybrid estimators

Assessments of the parametrized hybrid estimator schemes rely on the two validation data sets I and II, highlighted in Fig. 9. While the time-domain comparison (Fig. 11) offers a more vivid insight into the origin of emerging deviations, a lineup of quantitative measures (Fig. 12) provides a lucid view to assessing mode-wise and overall performance.

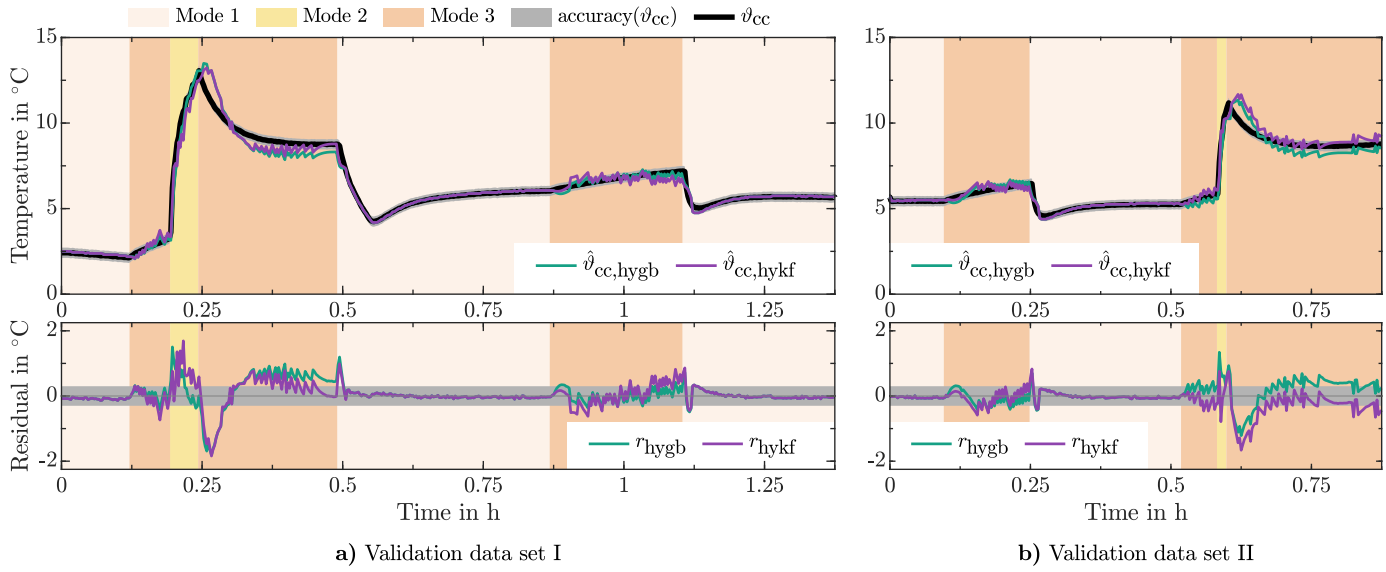

Fig. 11. Time-domain comparison of the performances of the hybrid estimators on (a) validation data set I and (b) validation data set II (Fig. 9 shows the affiliation of the validation data sets to the overall measurement data). Upper diagrams compare measurements ϑ_{cc} of the air temperature inside the cooling chamber with the estimates $\hat{\vartheta}_{cc}$ resulting from the two hybrid estimator approaches, while lower diagrams show associated residuals r.

In addition to the comparison of the estimation results with the measured value $\hat{\vartheta}_{cc}$, related residuals $r_i \in \mathbb{R}$, $i \in \{\text{hygb}, \text{hykf}\}$ according to:

$$r_i(k) := \vartheta_{cc}(k) - \hat{\vartheta}_{cc,i}(k) \tag{60}$$

indicate deviations clearly and allow identifying simply whether a certain approach over- or underestimates within particular periods. Quantitative overall and mode-wise ($m \in \{1,2,3\}$) comparison is, on the one hand, conducted by the root-mean-square error (RMSE) [48], according to

$$\text{RMSE}_i(m) := \sqrt{\frac{1}{n_V(m)} \sum_{j=1}^{n_V(m)} r_i^2(j)} \tag{61}$$

with $n_V(m)$ as the number of samples within mode m and both validation data sets, given as

$$n_V(m) := n_k(\text{I}(m)) + n_k(\text{II}(m)). \tag{62}$$

On the other hand, a relative measure of the performance of approach i is given by a value based on the normalized root-mean-square error [48], the Fit, according to

$$\text{Fit}_i(m) := 1 - \sqrt{\frac{\sum_{j=1}^{n_V(m)} r_i^2(j)}{\sum_{j=1}^{n_V(m)} \left(\vartheta_{cc}(j) - \bar{\vartheta}_{cc}(m)\right)}} \tag{63}$$

with the mean $\bar{\vartheta}_{cc}$ given as

$$\bar{\vartheta}_{cc}(m) = \frac{1}{n_V(m)} \sum_{j=1}^{n_V(m)} \vartheta_{cc}(j). \tag{64}$$

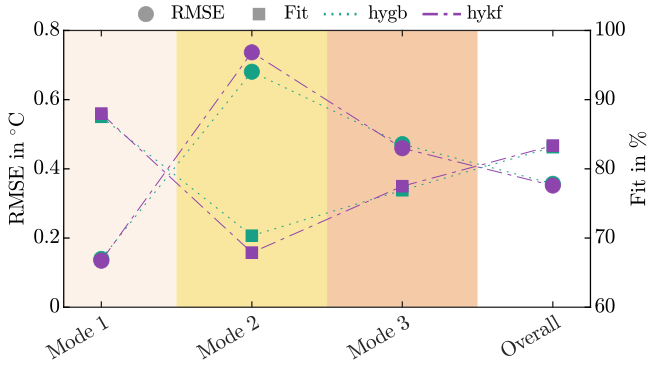

Fig. 12. Quantitative comparison of the performances of the hybrid estimators on the combined validation data, comprising data sets I and II according to Figs. 9 and 11. Performance values (RMSE and Fit) are separately presented for each operating mode as well as for the overall operation.

As handling operating mode 1 is identical in both estimation approaches, the quality of results is almost the same. Very slight differences, see mode 1 in Fig. 12, result from different initial conditions after switching back into mode 1. This is also apparent from the time-domain comparison presented in Fig. 11. Furthermore, peaks in the residuals directly after a switch back into mode 1 stem from the initially vestigial airflow directly after switching on the fan. Transition handling (40) reduces these deviations to a reasonable level.

During operating mode 2, both approaches indicate the least satisfactory performance compared with all other modes, see Fig. 12. The time-domain comparison indicates a delay that can be traced back to the comparably long sampling time with respect to the system dynamics in mode 2. Because of that, the exact time of door openings is inaccessible and captured delayed. Increasing the sampling rate is, therefore, highly recommended, would overcome this issue, and yield higher performance.

The most considerable absolute deviations arise after switching from mode 2 into mode 3 (Fig. 11) and result from the most significant change in the dynamics – from fast to slow. However, temperature deviations remain within a practicable range and decay rapidly over time. Noticeable differences in performance between both estimation approaches occur in mode 3 if a door opening happened beforehand. They result from slightly different initial conditions after switching from mode 2 into mode 3. Due to the comparably slower dynamics in mode 3, differences take longer to decay but eventually vanish.

All in all, although there are slight differences in all three modes, overall performances are practically identical to each other and show not only satisfactory results for the intended purpose but also compared with other temperature estimation approaches from literature [31,35]. Considering the uncertainty of measured values as a white noise process (see sensor accuracy in Table 2), prediction accuracy is not systematically affected. Nonetheless, it is worth pointing out that prediction

value, apparent in Fig. 12, is very close to the measured value to a certain extent. Additionally, in the residual plots of Fig. 11, comparing the predicted values with the range of sensor accuracy shows that deviations are mostly within this range. Note that the region of sensor accuracy is also depicted in the related temperature plots but remains barely visible as the plotted lines almost cover it. These comparisons furthermore indicate the modeling approach and estimation methods built upon that to be reasonable for the intended purpose.

However, operation in refrigerated trucks with much lower temperatures than discussed here may entail further research issues. As ice formation on the air chiller severely influences heat transfer, changes in system dynamics are highly conceivable. Therefore, more extensive experimental investigations with representative buildups of ice are favorable.

Compared with the experimental setup in this work, the thermal capacities of the cargo are not negligible in practical applications. Thus, heat transitions between cargo and air inside the cooling chamber influence local airflow and temperature close to the cargo. If the airflow is solely driven by natural convection (mode 3), the quality of the estimators might be reduced in the case of cargo types with excellent heat transfer and a severe temperature difference to the surrounding air. For such special applications, individual experiments are advisable to adapt the proposed algorithms appropriately.

As sensitive cargo may need more detailed insight into the temperature distribution, further research is needed to investigate the possibility of designing several estimators for different locations. Nonetheless, due to a vast number of primarily unknown parameters and initial temperature distributions of the cargo itself, the package, and many others, such attempts may only be promising for harshly restricting applications.

8. Conclusion

This work presents two model-based online strategies for estimating the air temperature close to the cargo in mobile, small-scale cooling chambers. In the face of frequent door openings and an extended, flexible architecture of the cooling unit, turning off the fan is more common than in typical state-of-the-art refrigeration applications. The proposed strategies overcome lack of knowledge about the inner air temperature in such periods by using available local temperature measurements within the cooling unit together with a simple lumped thermodynamic model. Experimentally-gained measurement data (total length: 14 h) obtained with a real-world refrigerated truck serve for parameterizing (data length: 11.75 h) the model and validating (data length: 2.25 h) both estimation approaches.

Both the Kalman-filter and the gray-box-model approach show satisfying results throughout all operating conditions. The overall fit to validation data is 83.4 % and 83.1 %, respectively. Although the Kalman-filter approach uses fewer model-related parameters, it requires a higher number of performance-related parameters than the gray-box-model approach. However, increased complexity comes along with enhanced flexibility and, therefore, a slightly better overall fit. Nonetheless, simplicity of the gray-box-model approach in design, operating, and maintenance facilitates its application vastly. The self-regulating property of the Kalman-filter approach is emulated within the more straightforward gray-box-model approach by implementing an additional method to handle transitions between different operating modes. Though complexities of the approaches differ from each other, standard microcontrollers can readily handle the computational burden of both. Based on the almost identical performance, straightforward design and simple maintenance of the gray-box-model approach outweigh the flexibility of the Kalman-filter approach in practical applications. Therefore, it is recommended to test the gray-box-model approach in a specific application in the first place and only switch to the more complex Kalman-filter approach if extended settings are essential for the overall performance.

Being aware of the temperature in periods characterized by a switched-off fan offers a wide range of benefits not just for classic but rather sophisticated control strategies. Utilizing the so-gained additional knowledge promises control schemes to improve overall efficiency and keep better track of given temperature restrictions throughout the whole operation. Hence, applying the proposed estimation approaches render heuristic and, in the best case, only suboptimal control actions during periods of otherwise uncertain temperature information unnecessary. Therefore, these methods constitute a cornerstone for applying comprehensive control strategies to the outlined flexible refrigeration units to finally decrease the amount of wasted goods, increase shelf-life, and lower economic and environmental costs in total. In light of the high number of refrigerated trucks worldwide, the potential impact of applying these methodologies is apparent.

Although the proposed methodologies only provide estimates for the air temperature close to the cargo, they significantly improve decision-making for control approaches compared with the uncertainty during periods with a switched-off fan in current applications.

Declaration of competing interest

The authors declare that they have no known competing financial interests or personal relationships that could have appeared to influence the work reported in this paper.

Acknowledgments

The continuing support and assistance of PRODUCTBLOKS GmbH in Korneuburg, Austria, in experimental investigations and data acquisition are gratefully acknowledged.

This work was supported by the Austrian Research Promotion Agency (Forschungsförderungsgesellschaft) by the project *DiNaMiC* [grant number 871303].

The authors acknowledge TU Wien Bibliothek, Austria for financial support through its Open Access Funding Programme.

References

[1] Refrigerated transport market by mode of transport (refrigerated road transport, refrigerated sea transport, and refrigerated rail transport), by temperature, by technology, by application (chilled food products and frozen food products), forecast to 2017–2027. Accessed: 2021-09-27. https://www.reportsanddata.com/report-detail/refrigerated-transport-market.

[2] Food and Agriculture Organization of the United Nations, Global food losses and food waste–extent, causes and prevention, 2011, http://www.fao.org/3/mb060e/mb060e00.htm, accessed: 2021-09-27.

[3] S.J. James, C. James, J.A. Evans, Modelling of food transportation systems – a review, Int. J. Refrig. 29 (6) (2006) 947–957, http://dx.doi.org/10.1016/j.ijrefrig.2006.03.017.

[4] A. Novaes, O. Lima Jr., C. Carvalho, F. Takebayashi, Thermal performance of refrigerated vehicles in the distribution of perishable food, Pesquisa Operacional 35 (2013) http://dx.doi.org/10.1590/0101-7438.2015.035.02.0251.

[5] S.E. Shafiei, A. Alleyne, Model predictive control of hybrid thermal energy systems in transport refrigeration, Appl. Therm. Eng. 82 (2015) 264–280, http://dx.doi.org/10.1016/j.applthermaleng.2015.02.053.

[6] Y. Huang, A. Khajepour, F. Bagheri, M. Bahrami, Optimal energy-efficient predictive controllers in automotive air-conditioning/refrigeration systems, Appl. Energy 184 (2016) 605–618, http://dx.doi.org/10.1016/j.apenergy.2016.09.086.

[7] E. Luchini, D. Radler, D. Ritzberger, S. Jakubek, M. Kozek, Model predictive temperature control and ageing estimation for an insulated cool box, Appl. Therm. Eng. 144 (2018) 269–277, http://dx.doi.org/10.1016/j.applthermaleng.2018.08.045.

[8] C.P. Tso, M.-C. Yu, H. Poh, P. Jolly, Experimental study on the heat and mass transfer characteristics in a refrigerated truck, Int. J. Refrig. 25 (2002) 340–350, http://dx.doi.org/10.1016/S0140-7007(01)00015-9.

[9] T. Lafaye De Micheaux, M. Ducoulombier, J. Moureh, V. Sartre, J. Bonjour, Experimental and numerical investigation of the infiltration heat load during the opening of a refrigerated truck body, Int. J. Refrig. 54 (2015) 170–189, http://dx.doi.org/10.1016/j.ijrefrig.2015.02.009.

[10] K. Wang, M. Eisele, Y. Hwang, R. Radermacher, Review of secondary loop refrigeration systems, Int. J. Refrig. 33 (2) (2010) 212–234, http://dx.doi.org/10.1016/j.ijrefrig.2009.09.018.

[11] J.M. Belman-Flores, S. Ledesma, D.A. Rodríguez-Valderrama, D. Hernández-Fusilier, Energy optimization of a domestic refrigerator controlled by a fuzzy logic system using the status of the door, Int. J. Refrig. 104 (2019) 1–8, http://dx.doi.org/10.1016/j.ijrefrig.2019.04.025.
[12] E. Luchini, A. Poks, D. Radler, M. Kozek, Model predictive temperature control for a food transporter with door-openings, in: 2020 SICE International Symposium on Control Systems (SICE ISCS), 2020, 85–91. http://dx.doi.org/10.23919/SICEISCS48470.2020.9083491.
[13] F. Borrelli, A. Bemporad, M. Morari, Predictive Control For Linear And Hybrid Systems, Cambridge University Press, 2017, http://dx.doi.org/10.1017/9781139061759.
[14] R.E. Kalman, A new approach to linear filtering and prediction problems, ASME J. Basic Eng. 82 (1960) 35–45, http://dx.doi.org/10.1115/1.3662552.
[15] T.P. Bohlin, Practical Grey-Box Process Identification: Theory And Applications, in: Advances in Industrial Control, Springer London, 2006.
[16] D. Simon, Optimal State Estimation: Kalman, H Infinity, And Nonlinear Approaches, Wiley-Interscience, USA, 2006.
[17] L. Fortuna, S. Graziani, A. Rizzo, M.G. Xibilia, Soft sensors for monitoring and control of industrial processes, Springer, London, 2007, http://dx.doi.org/10.1007/978-1-84628-480-9.
[18] P. Kadlec, B. Gabrys, S. Strandt, Data-driven soft sensors in the process industry, Comput. Chem. Eng. 33 (4) (2009) 795–814, http://dx.doi.org/10.1016/j.compchemeng.2008.12.012.
[19] G.C. Goodwin, K.S. Sin, Adaptive Filtering Prediction And Control, in: Dover Books on Electrical Engineering, Dover Publications, 2014.
[20] H. Tanizaki, Nonlinear Filters, Springer, 2014.
[21] Z. Wang, R. Kamyar, H. Mehdizadeh, P.Y. Pendse, Moisture soft sensor for agitated pan dryers using a hybrid modeling approach, Int. J. Pharm. 586 (2020) 119518, http://dx.doi.org/10.1016/j.ijpharm.2020.119518.
[22] G. Cogoni, Y.A. Liu, A. Husain, M.A. Alam, R. Kamyar, A hybrid NIR-soft sensor method for real time in-process control during continuous direct compression manufacturing operations, Int. J. Pharm. 602 (2021) 120620, http://dx.doi.org/10.1016/j.ijpharm.2021.120620.
[23] M. Kim, Y.-H. Lee, I.-S. Han, C. Han, Clustering-based hybrid soft sensor for an industrial polypropylene process with grade changeover operation, Ind. Eng. Chem. Res. 44 (2) (2005) 334–342, http://dx.doi.org/10.1021/ie049803b.
[24] E. Suzdaleva, I. Nagy, Online soft sensor for hybrid systems with mixed continuous and discrete measurements, Comput. Chem. Eng. 36 (2012) 294–300, http://dx.doi.org/10.1016/j.compchemeng.2011.09.004.
[25] T. Loussouarn, D. Maillet, B. Remy, V. Schick, D. Dan, Indirect measurement of temperature inside a furnace, ARX model identification, J. Phy. Conf. Ser. 1047 (2018) 012006, http://dx.doi.org/10.1088/1742-6596/1047/1/012006.
[26] G. Cosoli, P. Chiariotti, M. Martarelli, S. Foglia, M. Parrini, E.P. Tomasini, Development of a soft sensor for indirect temperature measurement in a coffee machine, IEEE Trans. Instrum. Meas. 69 (5) (2020) 2164–2171, http://dx.doi.org/10.1109/TIM.2019.2922750.
[27] A. Beghi, L. Cecchinato, Modelling and adaptive control of small capacity chillers for hvac applications, Appl. Therm. Eng. 31 (6) (2011) 1125–1134, http://dx.doi.org/10.1016/j.applthermaleng.2010.12.007.
[28] S.F. Fux, A. Ashouri, M.J. Benz, L. Guzzella, EKF Based self-adaptive thermal model for a passive house, Energy Build. 68 (2014) 811–817, http://dx.doi.org/10.1016/j.enbuild.2012.06.016.
[29] Z. O'Neill, S. Narayanan, R. Brahme, Model-based thermal load estimation in buildings, in: 2010 SimBuild, 2010.
[30] Z. Hao, Z. O'Neill, Model-based estimation of building infiltration, in: 2018 Building Performance Analysis Conference, 2018.
[31] Z. O'Neill, S. Narayanan, Model-based estimation of cold room temperatures in a supermarket refrigeration system, Appl. Therm. Eng. 73 (1) (2014) 819–830, http://dx.doi.org/10.1016/j.applthermaleng.2014.08.038.
[32] P. Radecki, B. Hencey, Online building thermal parameter estimation via Unscented Kalman Filtering, in: 2012 American Control Conference (ACC), 2012, 3056–3062. http://dx.doi.org/10.1109/ACC.2012.6315699.
[33] P. Radecki, B. Hencey, Online model estimation for predictive thermal control of buildings, IEEE Trans. Control Syst. Technol. 25 (4) (2017) 1414–1422, http://dx.doi.org/10.1109/TCST.2016.2587737.
[34] A.H. Raval, S.C. Solanki, R. Yadav, A simplified heat transfer model for predicting temperature change inside food package kept in cold room, J. Food Sci. Technol. 50 (2013) 257–265, http://dx.doi.org/10.1007/s13197-011-0342-z.
[35] R. Badia-Melis, U. Mc Carthy, I. Uysal, Data estimation methods for predicting temperatures of fruit in refrigerated containers, Biosyst. Eng. 151 (2016) 261–272, http://dx.doi.org/10.1016/j.biosystemseng.2016.09.009.
[36] C.C. Emenike, N.P. Van Eyk, A.J. Hoffman, Improving cold chain logistics through RFID temperature sensing and predictive modelling, in: 2016 IEEE 19th International Conference on Intelligent Transportation Systems (ITSC), 2016, 2331–2338. http://dx.doi.org/10.1109/ITSC.2016.7795932.
[37] R. Pedersen, J. Schwensen, B. Biegel, T. Green, J. Stoustrup, Improving demand response potential of a supermarket refrigeration system: A food temperature estimation approach, IEEE Trans. Control Syst. Technol. 25 (3) (2017) 855–863, http://dx.doi.org/10.1109/TCST.2016.2583958.
[38] L. Ljung, System identification: theory for the user, in: Prentice Hall information and system sciences series, Prentice Hall PTR, 1999.
[39] O. Nelles, Nonlinear system identification: from classical approaches to neural networks and fuzzy models, in: Engineering online library, Springer, 2001.
[40] MATLAB System Identification Toolbox, the MathWorks, Inc., Natick, Massachusetts, USA (R2020a) URL https://de.mathworks.com/products/sysid.html.
[41] Y. Ma, Y. Cui, H. Mou, J. Gao, H. Chen, Core temperature estimation of lithium-ion battery for EVs using Kalman filter, Appl. Therm. Eng. 168 (2020) 114816, http://dx.doi.org/10.1016/j.applthermaleng.2019.114816.
[42] Q. Jin, J.T. Wen, S. Narayanan, Dynamic control of microchannel cooling system with unanticipated evaporator heat loads, Appl. Therm. Eng. 183 (2021) 116225, http://dx.doi.org/10.1016/j.applthermaleng.2020.116225.
[43] R. Marchthaler, S. Dingler, Kalman-Filter: Einführung In Die Zustandsschätzung Und Ihre Anwendung für Eingebettete Systeme, Springer Fachmedien Wiesbaden, 2017.
[44] M. Bidarvatan, V. Thakkar, M. Shahbakhti, B. Bahri, A. Abdul Aziz, Grey-box modeling of HCCI engines, Appl. Therm. Eng. 70 (1) (2014) 397–409, http://dx.doi.org/10.1016/j.applthermaleng.2014.05.031.
[45] A. Aghababaei, M. Hexamer, Grey-box modeling of ex-vivo isolated perfused kidney, IFAC-PapersOnLine 48 (20) (2015) 171–176, http://dx.doi.org/10.1016/j.ifacol.2015.10.134, 9th IFAC Symposium on Biological and Medical Systems BMS 2015.
[46] Datasheet Dallas DS18S20. 2020. otom Group GmbH, Bräunlingen, Germany. https://www.sensorshop24.de/kabelfuehler-durchmesser-6mm.
[47] Datasheet 3-wire Pt100. 2020. otom Group GmbH, Bräunlingen, Germany, https://www.sensorshop24.de/lufttemperaturfuehler.
[48] A. Botchkarev, Performance metrics (error measures) in machine learning regression, forecasting and prognostics: Properties and typology, 2018, ArXiv, arXiv:1809.03006.